Progress in Additive Manufacturing
https://doi.org/10.1007/s40964-026-01876-5

RESEARCH

Unveiling crack mitigation pathways in powder bed fusion–laser beam of CM247LC: an *operando* X-ray radiography study of Hf and nano-Y_2O_3 additions

Ahmed Fardan[1] · Gowtham Soundarapandiyan[1,2] · Vigneashwara Pandiyan[3,4] · Steven Van Petegem[5] · Efthymios Polatidis[6] · Sofia Kazi[1] · Sneha Goel[5,7] · Camille Pauzon[1,8] · Federica Marone[9] · Bharat Mehta[10] · Annapaola Parrilli[11] · Håkan Brodin[1,12] · Eduard Hryha[1]

Received: 30 November 2025 / Accepted: 16 July 2026

Abstract

Cracking presents a major hurdle for processing non-weldable Ni-base superalloys, such as CM247LC, by powder bed fusion–laser beam (PBF–LB). This study directly observes cracking behavior in standard CM247LC and two admixed alloys (CM247LC + 1 wt.% Hf and CM247LC + 1 wt.% nano-Y_2O_3) using *operando* synchrotron X-ray radiography synchronized with acoustic emission (AE). Our real-time data confirm extensive cracking in the standard alloy is identified to be primarily solidification cracking. Both Y_2O_3 and Hf additions mitigate solidification cracking, though through distinct mechanisms. Nano-Y_2O_3 addition alters the processing regime from keyhole to conduction mode. Scheil solidification simulations predict a narrower solidification range and lower solidification cracking index (SCI). This indicates that a combination of processing regime shift along with modification in solidification as the primary drivers for crack suppression upon addition of nano-Y_2O_3, despite increased lack of fusion and complex oxide formation. Hf-addition mitigated cracking via enhanced segregation at interdendritic regions, promoting beneficial carbides and improved liquid backfilling. Scheil simulations for alloy with Hf-addition predicted low SCI compared to standard CM247LC due to increased liquid availability in final solidification stages. These insights highlight that nearly crack-free PBF–LB of non-weldable superalloys can be achieved through both the powder modifications.

Keywords Solidification cracking · Ni-base superalloy · Powder modification · *Operando* radiography · PBF–LB · CM247LC · X-ray computed tomography

1 Introduction

Additive manufacturing (AM), particularly powder bed fusion–laser beam (PBF–LB), has revolutionized component fabrication by enabling creation of complex three-dimensional geometries layer-by-layer. This unparalleled design freedom is highly attractive to demanding industries such as aerospace and energy sectors utilizing gas turbine systems, where intricate internal cooling channels within burners, guide vanes and turbine blades can significantly enhance engine efficiency, extend component lifetime, and optimize cooling air utilization. Ni-base superalloys, strengthened by the γ′ precipitate with an $L1_2$ crystal structure ($Ni_3(Al,Ti)$), are extensively employed in high-temperature sections of gas turbines due to their exceptional resistance to high-temperature corrosion/oxidation and creep. While a high volume fraction of γ′ (typically 60 to 70 vol.%) is desirable for superior mechanical properties, it often renders these alloys, such as CM247LC, susceptible to (hot) cracking during PBF–LB processing.

Hot cracks are broadly categorized into two types: solidification cracking and liquation cracking. Solidification cracks form in the final stages of melt pool solidification when tensile stresses pull apart residual solute-rich liquid in the interdendritic regions [1]. Liquation cracks, on the other hand, originate from localized melting of low melting

Extended author information available on the last page of the article

Published online: 03 August 2026

phases and segregations in heat-affected zone (HAZ), which then tear apart under thermal strains [1]. Distinguishing these two crack types using conventional post-mortem electron microscopy can be challenging, as both can exhibit similar solidification characteristics on their surfaces [2, 3]. Although some studies have linked smaller liquation cracks (~2–3 µm in length) to reheated MC carbides or eutectic phases [4], or larger liquation cracks (~30–40 µm) with smooth, wavy surfaces contrasting dendritic solidification cracks [5], however definitive differentiation remains difficult. This inherent ambiguity highlights the critical need for real-time monitoring methods capable of observing crack formation during PBF–LB.

Recent advancements in *operando* synchrotron X-ray radiography have demonstrated the capability to monitor cracking in alloys like CM247LC in real time, overcoming the limitations of post-mortem analysis [6]. Such studies have confirmed the simultaneous occurrence of both solidification and liquation cracks occurring during processing, with liquation cracks sometimes exhibiting lengths comparable to solidification cracks (~40 µm), supporting earlier post-mortem observations [5, 6].

To mitigate these pervasive cracks in CM247LC and similar alloys, various strategies have been explored. Process parameter optimization, for instance, by reducing line energy density to promote shallower melt pools, can minimize cracking by promoting a crystallographic texture with reduced grain boundary misorientation [2, 7, 8]. However, this approach often compromises productivity and increases manufacturing costs, or restricts the process window flexibility which is an inherent advantage of PBF–LB. As such, further exploration into alloy-specific solutions is required to overcome these restrictions.

Indeed, alloy modification represents a promising avenue. On the one hand, some studies have explored removing Hafnium (Hf) in CM247LC, [9, 10], such modifications can possibly impact crucial high-temperature mechanical and oxidation properties given Hf's vital role in superalloys. Hf is known to improve solid solution strengthening [11], strengthen grain boundaries (by influencing MC and $M_{23}C_6$ carbides), influence γ′ morphology and stability, and enhance oxidation resistance [11, 12]. Furthermore, Hf additions (up to 2 wt.%) have prevented grain boundary cracking in directionally solidified cast Ni-base superalloys by promoting a more gradual change in liquid volume fraction during solidification, thereby reducing strains in the critical temperature interval [13]. More recently, Hf addition in IN738LC (an alloy typically without Hf) effectively eliminated solidification cracking by ensuring cracks were filled with Hf-rich liquid in the final solidification stages [14]. Therefore, investigating the influence of Hf on solidification cracking in CM247LC, where it is already a nominal constituent, offers particularly relevant insights.

On the other hand, the addition of nanoparticles also offers a novel approach to minimize hot cracking in crack-prone alloys. For example, TiC nanoparticles have been shown to reduce hot cracks in non-weldable IN738LC superalloy [15, 16]. This was attributed to the promotion of equiaxed microstructures, shallower and wider melt pools, and altered thermal conductivity within the melt pool [16]. Similarly, Y_2O_3 nanoparticles have shown benefits in crack mitigation, though the underlying mechanisms reported in literature vary. Guo et al. [17] demonstrated that Y_2O_3 reacted with IN738LC to form crack-suppressing $Y_4Al_2O_9$ slags with Zr enrichment. Conversely, Kenel et al. [18] reported that Y_2O_3 reacted with a Ni–Cr–Al–Ti (model alloy based on CM247LC) to form $Y_4Al_2O_9$ and Y–O–S dispersoids, but also detrimental eutectic Y–Ni intermetallics ($Ni_{17}Y_2$) along grain boundaries, leading to increased cracking. Such studies also reported increased porosity and slag formation with Y_2O_3 additions [18]. These disparate findings highlight the complex role of nanoparticles and the need for a deeper understanding of their interactions in PBF–LB.

Bulk acoustic emissions are transient elastic waves that propagate through the solid material or build substrate after rapid internal stress redistribution. In laser-based additive manufacturing with AM, such waves can arise from crack opening, crack propagation, thermal contraction, phase transformation, dislocation motion, and other microstructural events. Because these processes are directly linked to solidification, post-solidification cooling, and stress accumulation, bulk AE provides a useful high-time-resolution route for characterizing solidification behaviour and crack-related activity. Acoustic sensors can detect these waves, offering valuable insight into transformation and cracking kinetics by analysing signal characteristics such as amplitude, frequency content, and event timing.

Recent acoustic-emission-based studies in laser additive manufacturing show that AE is sensitive to rapid stress-release events, including crack initiation, crack propagation, phase transformation, dislocation activity, and thermally induced deformation. Song et al. showed that AE signals during laser–powder interaction can be separated according to source mechanisms such as tensile cracks during cooling, powder-related effects, and rapid thermal expansion; importantly, crack-related AE events were impulsive, high-frequency-rich, and occurred mainly after laser shut-off [19]. Raeker et al. further demonstrated that, during laser-melting screening of AM alloys, piezoelectric AE could detect individual solid-state cracking events in TZM (titanium-zirconium-molybdenum), while hot-tearing/solidification cracking in CMSX-4 was not detected under their experimental configuration, highlighting the strong

dependence of AE detectability on crack mechanism, emitted acoustic energy, sensor bandwidth, and coupling path [20]. Beyond direct crack detection, AE has also been used to monitor microstructural transformations during laser processing. Esmaeilzadeh et al. showed that structure-borne AE in PBF–LB of Ti6Al4V–Fe captured signatures associated with martensitic transformation and post-laser crack formation, indicating that acoustic sensors can detect waves generated by transformation-related energy release and provide insight into transformation kinetics through signal amplitude, frequency, and timing [21]. Similarly, Navarre et al. correlated AE with *operando* X-ray diffraction during laser-induced recrystallization and demonstrated that AE can track microstructural events such as dislocation rearrangement, nucleation, and grain growth [22]. In directed energy deposition (DED), Ansari et al. showed that AE can detect both surface and subsurface crack activity, including delayed crack formation after laser interaction, consistent with residual-stress accumulation and post-solidification crack growth [23]. Bevans et al. further demonstrated the value of build-plate-mounted AE sensors in PBF–LB for monitoring subsurface phenomena, noting that AE can capture elastic waves generated by cracks, phase transformations, dislocation activity, deformation, and thermally induced defects [24]. Taken together, these studies indicate that AE is well suited for identifying transient crack-associated activity in laser-based AM; however, mechanism assignment requires correlation with independent ground-truth measurements such as *operando* radiography, diffraction, microscopy, or thermal-state estimation.

Building on these prior studies on CM247LC and related crack-prone superalloys, the present work makes two main contributions. First, we directly link operando synchrotron X-ray radiography with synchronized structure-borne AE sensors to track individual crack initiation and growth events in CM247LC during PBF–LB, providing a time-resolved view of solidification cracking and its acoustic signatures. Second, we compare two targeted powder-modification strategies (additions of 1 wt.% Hf and 1 wt.% Y_2O_3) within the same experimental (radiography and post-mortem microstructural analysis) and thermodynamic simulation framework, showing that the crack suppression occurs through distinct mechanisms involving melt-pool regime changes, and altered solidification behavior, supported by non-equilibrium Scheil simulations. These findings provide critical insights for future alloy design and process optimization in additive manufacturing with AM of crack-prone alloys.

Table 1 Chemical composition of the Standard CM247LC powder used in this study

	Cr	Co	Mo	C	W	Hf	Ta	Ti	Al	Zr	B	Ni
wt.%	8	9.3	0.5	0.06	9.7	1.3	3.2	0.8	5.6	0.009	0.01	Bal

2 Methodology

2.1 Materials and powder characterization

This study utilized commercially available argon gas atomized CM247LC powder (Höganäs AB, Höganäs, Sweden) with a particle size range of 15 to 45 µm as the baseline material. The chemical composition, as provided by the supplier, is detailed in Table 1. Two additional powder variants were prepared by separately admixing 1 wt.% pure Hf and 1 wt.% nano-Y_2O_3 to the base CM247LC powder. These additives, sourced from US Research Nanomaterials Inc. (Houston, TX, USA), had particle size ranges of 30 to 45 µm for Hf, and 20 to 45 nm for nano-Y_2O_3. Powder blending was performed for 4 h for each variant using a low-speed blender to ensure adequate mixing. Hereafter, these three powder variants will be referred to as Standard, Standard + Hf and Standard + Y_2O_3.

Powder morphology was examined using a Zeiss Gemini 450 SEM (Carl Zeiss Microscopy GmbH, Oberkochen, Germany), equipped with an in-lens detector, and operated with an accelerating voltage of 10 kV, probe current of 100 pA and working distance of 8.5 mm. The samples were prepared by lightly pressing the powder on pure Al plates (99.9% Al).

Powder absorptivity at NIR-laser wavelengths was measured for all the three powder variants. Diffuse reflectance was quantified using a Shimadzu UV-2600 spectrophotometer equipped with an ISR-2600Plus Integrating Sphere attachment. The Kubelka–Munk (K–M) transformation was applied to each wavelength point in the diffuse reflectance (R) spectrum to obtain the K–M unit, F(R), which is proportional to laser absorptivity.

2.2 *Operando* PBF–LB experiment set-up

To understand the effects of powder blending on laser-matter interaction, and cracking and its inhibition, *operando* high-speed X-ray imaging experiments were conducted using a miniature PBF–LB device (MiniSLM, shown in Fig. 1a, b) at an X-ray imaging beamline. More information provided in Sect. 2.4. A detailed description of the MiniSLM can be found in references [25, 26].

For each powder condition, thin walls approximately 4 mm long, 0.15 mm thick, and 1 mm high were printed on a Ni-base superalloy Alloy 718 base plate. These walls were fabricated using three scan vectors to form a base for subsequent *operando* radiography. A perimeter wall was printed on top of this base to create a groove. This groove (4 mm long × 0.05 mm thick × 0.04 mm high) was manually filled with the test powder, and the perimeter wall served as a guide for the subsequent single-track deposition with

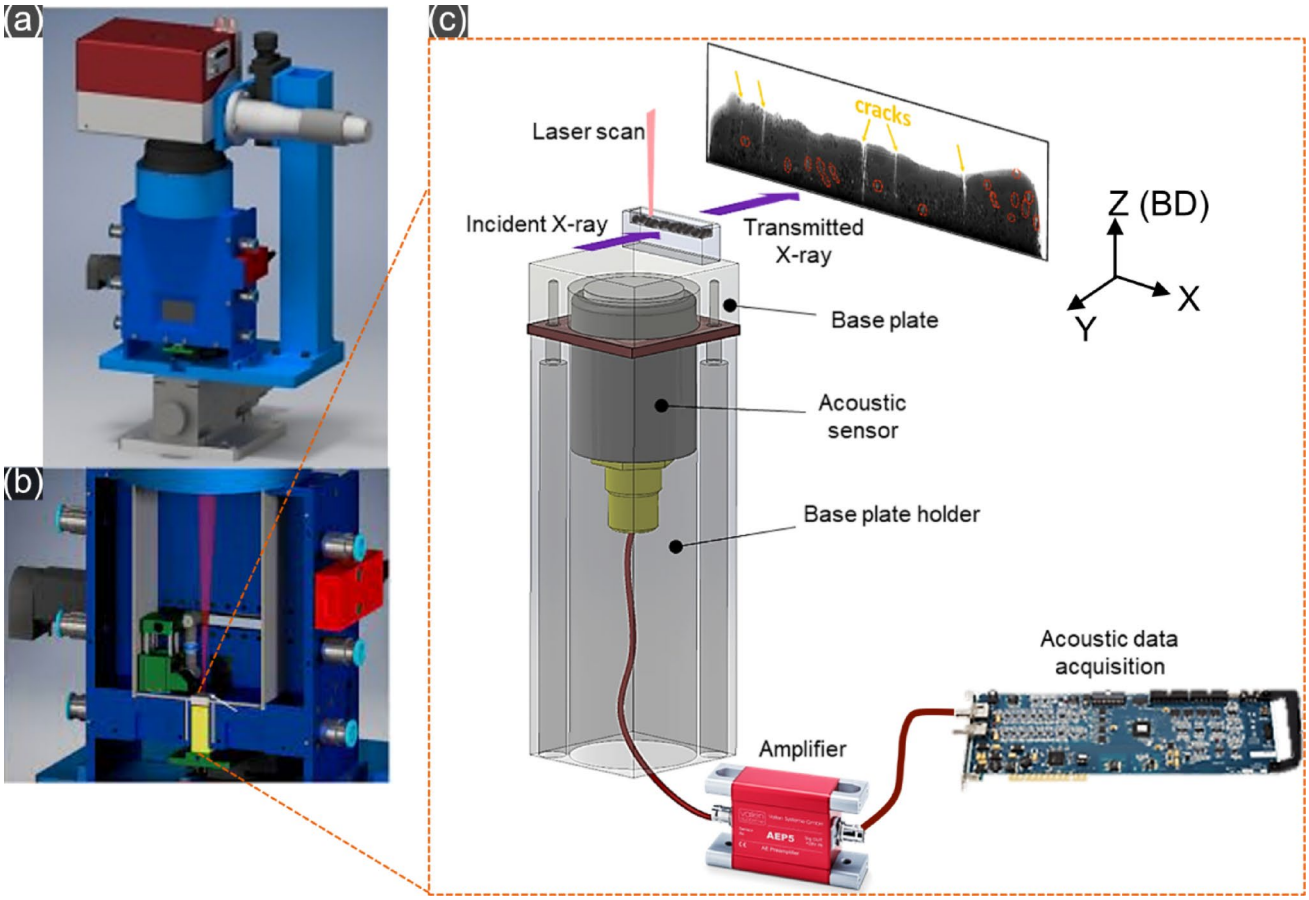

Fig. 1 Schematic of the miniaturized PBF–LB machine (MiniSLM) **a** exterior [26], **b** interior [26], and **c** operando radiography and acoustic emission acquisition set-up

Table 2 PBF–LB processing parameters used during operando X-ray radiography

Power (W)	100
Scanning speed (mm/s)	200
Layer thickness (µm)	40
Beam diameter (µm)	50

simultaneous radiography. All printing was carried out under argon atmosphere with oxygen levels below 0.12% in the print chamber.

Operando X-ray radiography was performed on a single-track deposition (40 µm layer thickness, 4 mm length) made using the printing parameters detailed in Table 2, which were kept identical for all the three powders. These parameters were determined based on prior ex-situ analyses on Standard powder. A relatively slow scanning speed was selected to meet the imaging conditions of the beamline and to facilitate better visualization of the physical phenomena during laser-powder interaction in PBF–LB process. The laser power was concurrently reduced to compensate for the adjusted energy input. It is to be noted that groove/thin wall set-up for operando radiography and the slow scan speed (200 mm/s) do not fully represent industrial processing where typically higher speeds (~1200–1500 mm/s) and relatively bulky components are built.

2.3 Acoustic emission monitoring

The MiniSLM system underwent targeted modifications to its baseplate, holder, and stage to accommodate a structure-borne acoustic emission (AE) sensor, the VS370-A3 (Vallen Systeme, Wolfratshausen, Germany), as illustrated in Fig. 1c [27]. The VS370-A3 is a passive piezoelectric AE sensor characterized by a compact form factor with threaded housing, top-mounted connector, and ceramic wear plate. It is specifically designed for secure installation using a screw-in mounting mechanism. In this configuration, the sensor was rigidly mounted to the underside of the baseplate with the aid of an acoustic couplant to ensure efficient transmission of stress waves. The sensing element of the VS370-A3 is oriented to be sensitive to stress wave propagation in the longitudinal direction relative to the sensor body which is an essential condition for accurately capturing structure-borne acoustic emissions generated during the process. The

couplant plays a critical role in establishing effective acoustic coupling and minimizing acoustic impedance mismatch between the sensor and the baseplate. This setup reduces signal attenuation and enhances the fidelity of stress wave detection originating in the bulk from the laser-material interaction zone.

This configuration remained consistent for the processing of all three powder types in the study. The VS370-A3 sensor is designed with a frequency sensitivity range spanning from 100 to 600 kHz. This operational bandwidth inherently suppresses low-frequency noise originating from ancillary machine components such as the recoater, powder flow dynamics, spatter events, and stage movements, thereby enhancing signal quality for process-relevant AE events. A 750 kHz low-pass filter was applied to satisfy the Nyquist criterion for the 1.5 MHz sampling rate, while fully covering the effective sensor bandwidth and attenuating higher-frequency noise. Accurate synchronization between the laser trigger and the AE signal acquisition was imperative for meaningful data capture. This was accomplished using a data acquisition (DAQ) system equipped with an Advantech 1840 PCIe DAQ card. The DAQ system operated with two synchronized channels, each supporting a dynamic range of ± 5 V. Channel 1 was configured to receive real-time laser on/off signals directly from the laser's control circuitry, providing precise temporal markers for the start and end of each scan track. Concurrently, Channel 2 was dedicated exclusively to acquiring the AE sensor output, ensuring that AE data was accurately aligned with laser activity.

A sampling rate of 1.5 MHz was employed to satisfy the Nyquist–Shannon sampling criterion, ensuring accurate capture of AE signals up to the maximum frequency limit of the sensor. This corresponds to a temporal resolution of 0.667 microseconds per sample, enabling the detection of high-speed transient stress wave events with sub-microsecond precision. From each scan track, the AE dataset was segmented into time windows of 3.3 ms. Each 3.3 ms segment consisted of 5000 discrete data points, providing sufficient temporal resolution to capture the dynamic acoustic signatures associated with the process. Following data acquisition, the raw AE signals were subjected to offline processing using a low-pass Butterworth filter with a cut-off frequency of 750 kHz. This filter setting was selected to align with the upper bound of the AE sensor's frequency response, effectively attenuating out-of-band noise while preserving the integrity of the process-relevant AE signals.

To identify post-laser AE events, the filtered AE waveform was analysed using a moving root-mean-square (RMS) energy metric and a short-term average/long-term average (STA/LTA) representation. The RMS trace was used as a crack-intensity indicator, where transient events were defined as localized post-laser peaks exceeding the background level of the filtered signal. The STA/LTA ratio was additionally used to distinguish short-duration burst-like acoustic events from the slowly varying process background. Events detected by both RMS energy and STA/LTA response were treated as consensus AE events and correlated with crack evolution observed in the synchronized operando radiographs.

2.4 Synchrotron X-ray radiography

Operando radiography experiments were performed at the TOmographic Microscopy and Coherent rAdiology experimenTs (TOMCAT) beamline of the Swiss Light Source (SLS) at Paul Scherrer Institute (PSI) in Switzerland. A polychromatic X-ray beam with a peak energy of 20 keV was utilized. After interacting with the melt pool, the attenuated X-rays were converted to visible light by a 150 µm thick LuAG:Ce scintillator and captured by a high numerical aperture microscope (4 × magnification; Optique Peter, Lentilly, France). The radiographs were recorded using an in-house developed GigaFRoST detector [28]. The effective pixel size for the radiographs was 2.75 µm, and images were captured at a high frame rate of 10 kHz.

2.5 X-ray computed tomography

X-ray computed tomography (XCT) measurements were performed on samples following the synchrotron measurements using an EasyTom XL Ultra 230–160 micro/nano-CT scanner (RX Solutions, Chavanod, France), equipped with a Varian PaxScan 2520DX flat panel detector. Scanning was carried out in continuous stack mode over three full rotations, with the voltage set to 200 kV and the current set to 75 µA. A frame rate of 8 and a frame averaging of 10 were used. The voxel size was set to 2.50 µm, based on the selected magnification geometry. CT images were reconstructed using RXAct software (RX Solutions), with slicing performed along the plane of interest.

2.6 Microstructural characterization

For microstructural investigation, the build plate was sectioned along the laser scanning direction (XZ plane in Fig. 1) with some clearance containing the build plate material. The cross-sections, along with the build plate, were glued to a cylindrical sample and then mounted on Accu-Stop from Struers for controlled manual grinding. Grinding commenced with 800-grit SiC paper until the build plate was removed and the sample cross-section was fully exposed. This was followed by sequential grinding with 1000, 1200, 2000, and 4000-grit SiC papers. Polishing was then performed using a 3 µm diamond suspension on

a taffeta woven wool surface (MD-Mol by Struers), followed by a 1 µm polishing step. Finally, a 0.05 µm colloidal silica (OPS) suspension was used to remove any residual deformation from previous grinding and polishing steps. The prepared cross-sections were then examined using a Zeiss Gemini 450 SEM (Carl Zeiss Microscopy GmbH, Oberkochen, Germany) with secondary electron (SE) and backscattered electron (BSE) detectors.

2.7 Simulations

Thermo-Calc 2025b software and the TCNI13 database were employed to perform Scheil solidification simulations. This database improves the description of phase equilibria involving Sigma and/or Mu phases in several binary and ternary systems by Effective Bond Energy Formalism (EBEF). The default phases in the TCNI13 database were used, with the sole exception of incorporating the M2O3_C phase (representing the Y_2O_3 phase) for the Standard + Y_2O_3 calculations. Scheil with solute trapping model based on Aziz's work [29] was utilized. For the solute trapping model, the scanning speed was defined as 200 mm/s and the angle between solid–liquid interface and scanning direction (alpha) was defined as 45°. Primary phase was selected to be FCC_L12 (γ matrix phase) to capture solute trapping in primary phase accurately. For Standard + Y_2O_3 simulation, Y and O were added to the alloy representing ~ 0.7 wt% Y_2O_3, increasing which caused numerical issues with Scheil simulations. A reason for adding O separately instead of stoichiometric Y_2O_3 is making some O available in liquid to form other oxide phases (as observed Hf, Al-oxides in the as-printed microstructure [2]) while not affecting stability of other solidifying phases. A modified cut-off criteria of 0.06 fraction of liquid was taken instead of default 0.01 (only for Standard + Y_2O_3 case) in order to successfully run the simulations.

3 Results and discussion

3.1 Powder characteristics

SEM micrographs of the three powders (Standard, Standard + Hf, and Standard + Y_2O_3) are presented in Fig. 2. SEM micrographs of the admixed powders (Fig. 2e, f) clearly showed loosely adhered, non-spherical micro-sized Hf particles and nano-sized Y_2O_3 particles (inset of Fig. 2f) deposited on the surface of the spherical CM247LC particles. Point energy dispersive spectroscopy (EDS) analyses of these features confirmed their elemental composition as Hf (Fig. 2h) and Y_2O_3 (Fig. 2i), respectively. The absorptivity results (Fig. 2g) indicated that the laser absorbance was highest for Standard + Hf powder followed by Standard + Y_2O_3 and least for the Standard powder.

3.2 *Operando* observations of crack formation and mitigation

Operando synchrotron X-ray radiographs and synchronized acoustic emission (AE) monitoring (Fig. 3) provided real-time insights into the cracking behavior of CM247LC during powder bed fusion–laser beam (PBF–LB). Observations demonstrate that Standard CM247LC is highly susceptible to cracking, while additions of Hf and Y_2O_3 effectively mitigate crack formation under identical processing conditions.

For the Standard CM247LC, radiographs (Fig. 3a, Supplementary Movie 1) reveal that cracks are primarily solidification cracking. This is a type of hot cracking and has been extensively documented in the literature for CM247LC [4, 5]. Most of the cracks observed from the radiographs in Fig. 3a and Supplementary Movie 1 appear to be solidification cracks, as they consistently form after the laser pass and during the solidification process. An example of this dynamic cracking behavior is captured at the 2.3 ms timestamp, where a crack partially remelts, then reforms and grows rapidly between 5.6 ms and 6.2 ms. Interestingly, some cracks do not regrow after remelting. However, controlled remelting is a potential strategy for minimizing solidification cracks in CM247LC, a technique successfully demonstrated for other solidification crack-prone alloys [30, 31]. Interestingly, no clear evidence of liquation cracking could be observed from the radiographs.

Analysis of the AE signal for Standard CM247LC shows that the signal amplitude is highest during the laser-on period, as expected from active laser–material interaction, but a decaying transient response persists immediately after laser shut-off. Within this post-laser interval, localized burst-like spikes are still evident, distinguishing them from the lower-amplitude background signal. As these spikes occur after laser shut-off and coincide in time with crack-related features observed in the *operando* radiographs, such as crack initiation, partial remelting, and subsequent rapid growth, they are consistent with crack initiation and/or propagation events during the final stages of solidification. Frequency-domain analysis further shows that the dominant acoustic activity is concentrated primarily within the 150 to 450 kHz range, with the strongest contribution in the 300 to 450 kHz band, while spectral intensity above 600 kHz remains weak (Fig. 4a). The spectrogram confirms that these high-intensity components are temporally localized rather than stationary, including during the post-laser interval (Fig. 4b). Notably, these localized high-energy bands align with the time window in which dynamic crack evolution is observed in the radiographs, indicating that the AE

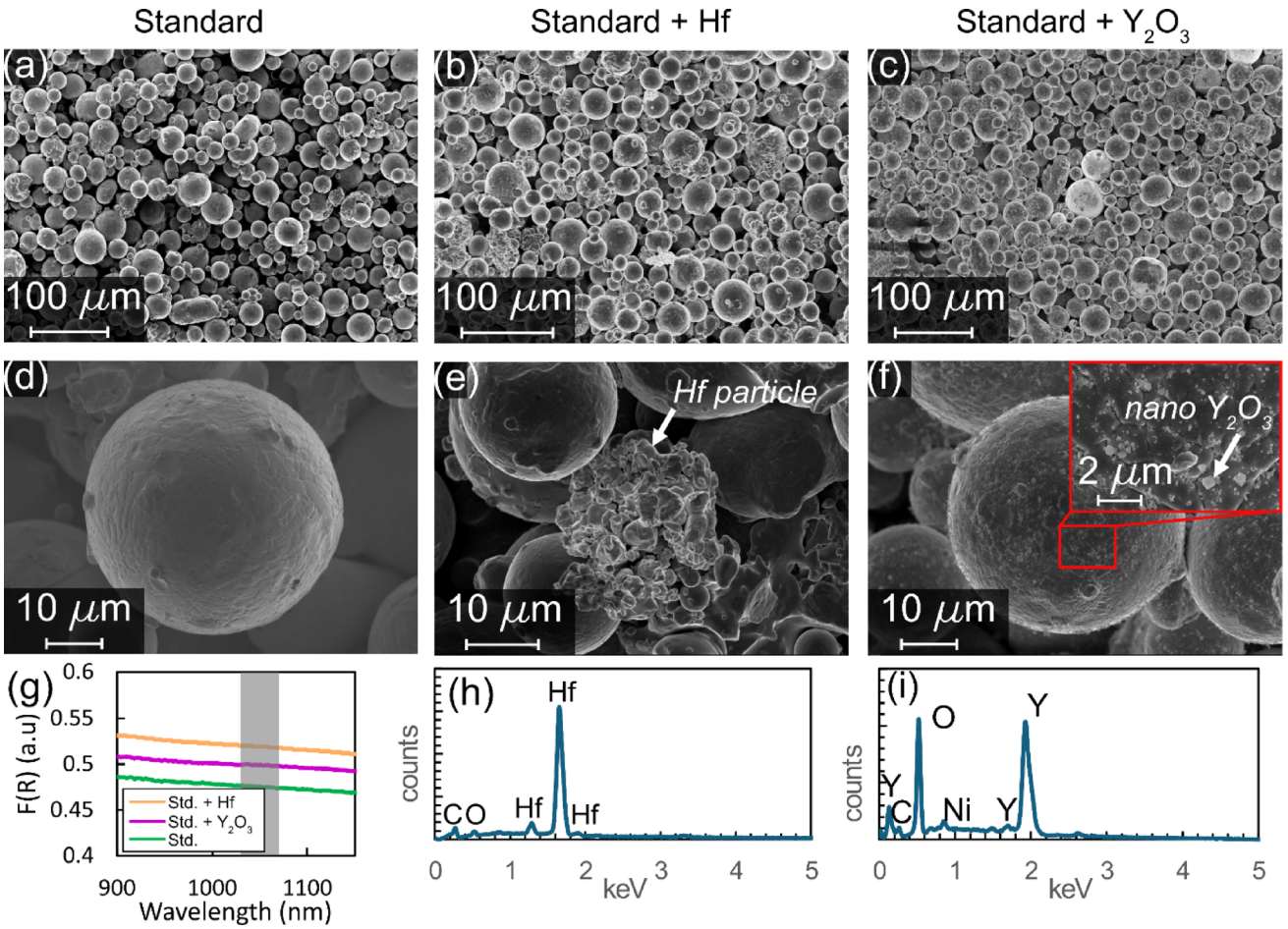

Fig. 2 SEM micrographs of powder particles for **a**, **d** Standard, **b**, **e** Standard + Hf and **c**, **f** Standard + Y_2O_3. **h** and **i** point EDS spectra of Hf and Y_2O_3 particles, respectively. **g** Kubelka–Munk transform, F(R), of the diffuse reflectance which is proportional to laser absorptivity. The wavelength of the laser (1030–1070 nm) is indicated by the grey region. Std. refers to Standard

response captures discrete, transient events rather than continuous process noise. Together, these observations indicate that the AE response of Standard CM247LC is governed by transient high-energy events, with crack-associated activity primarily falling within the 150 to 450 kHz range, and most prominently within the 300 to 450 kHz band.

Additionally, the synchronized AE signal (Fig. 3a) indicates that the spikes can be correlated with the solidification cracks that occur after the laser is switched off, at timestamps between 20.1 and 35 ms (Supplementary Movie 1). This direct correlation validates AE as a sensitive real-time indicator of cracking events. To further examine the post-laser crack-related AE activity, the filtered AE waveform was analyzed using a moving RMS energy metric together with time–frequency representations and a consensus crack map (Fig. 5). A clear drop in overall AE amplitude is observed immediately after laser shut-off in the filtered AE signal (Fig. 5b), followed by discrete post-laser burst events that remain above the background level in the RMS-based crack intensity trace (Fig. 5c). Using this RMS-based trace, the first post-laser event appears at approximately 2.2 ms after laser shut-off, followed by subsequent events extending up to about 10.2 ms, with weaker delayed activity visible up to about 13.0 ms (Fig. 5c). The spectrogram shows that these post-laser bursts are temporally localized rather than stationary and remain concentrated mainly in the same frequency window identified from the spectral analysis, i.e., predominantly within 150 to 450 kHz, with the strongest activity around the 300 to 450 kHz band (Fig. 5d). The STA/LTA representation, shown in Fig. 5e, was used to detect transient acoustic events. It compares the short-window signal energy, which captures rapid burst-like changes, with the long-window signal energy, which represents the local background response. The STA/LTA value is therefore calculated as the ratio between these two moving averages, with sudden increases indicating transient AE events. Sudden increases in this ratio indicate transient events such as crack-related acoustic bursts. In parallel, the STA/LTA map enhances these post-laser disturbances and suppresses the comparatively steady laser-on response, thereby improving

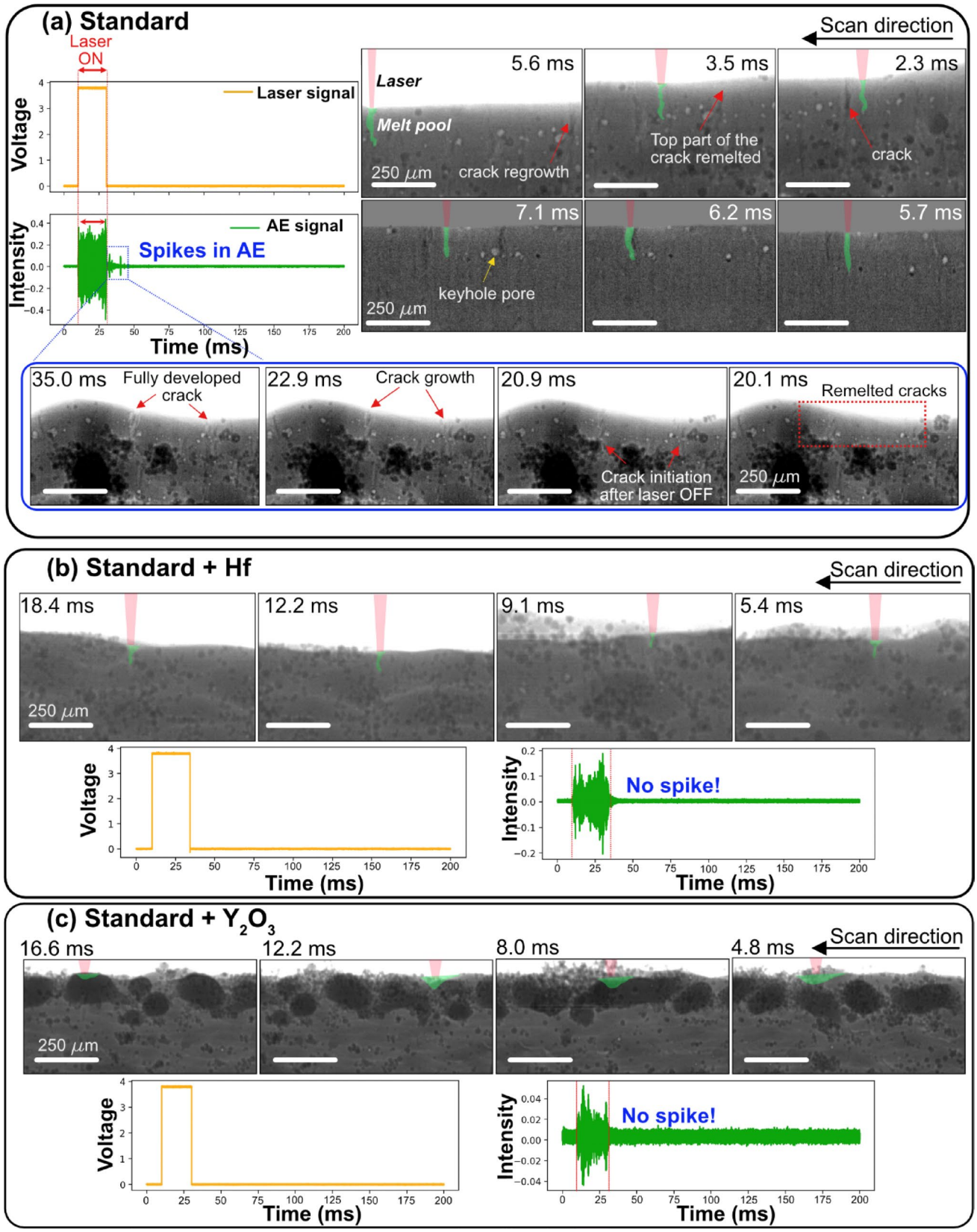

Fig. 3 Radiographs acquired during PBF–LB process and corresponding AE signals for the three powders **a** Standard, **b** Standard + 1 wt.% Hf, **c** Standard + 1 wt.% Y_2O_3. See Supplementary Movie 1, Supplementary Movie 2 and Supplementary Movie 3 for detailed observation

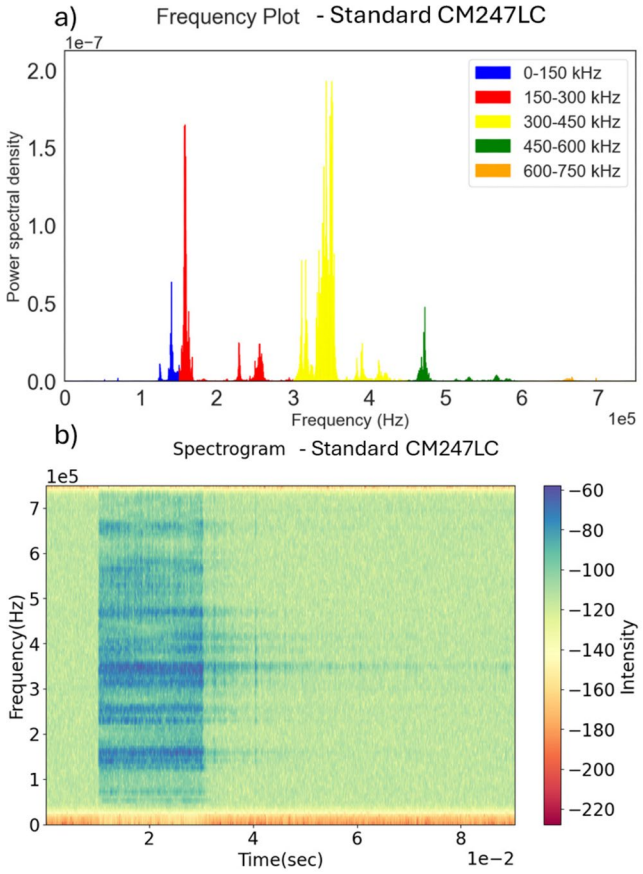

Fig. 4 Frequency- and time–frequency-domain analysis of acoustic emission (AE) signal for Standard CM247LC during PBF–LB: **a** power spectral density showing dominant frequency bands, and **b** spectrogram illustrating temporal localization of high-energy acoustic activity

separation of crack-associated events from the process background (Fig. 5e). The final consensus crack map identifies two dominant post-laser crack events at approximately 2.2 ms and 10.2 ms after laser shut-off (Fig. 5f), which is consistent with the crack-related transient activity observed in the *operando* radiographs. Together, these results further support that the AE response of Standard CM247LC after laser shut-off is governed by discrete crack initiation and/or propagation events during the final stages of solidification.

In contrast, with the addition of 1 wt.% Hf (Fig. 3b, Supplementary Movie 2) and 1 wt.% Y_2O_3 (Fig. 3c, Supplementary Movie 3), no cracks were observed in the radiographs. Moreover, the AE signals showed no discernible spikes after the laser was switched off. However, the reason for the crack elimination with these additions appear different, as evidenced by their distinct effects on melt pool shape/geometry. Figure 3b and Table 3 shows that the addition of Hf leads to a decrease in the melt pool depth (Standard: 154 ± 17 µm and Standard + 1 wt.% Hf: 74 ± 6 µm). The melt pool geometry (Table 3) along with the post-build XCT measurements (Fig. 8 in Appendix A), it is observed that there is a transition from keyhole mode to transition-like mode with Hf addition. This change in mode is primarily based on the absence of keyhole pores for the Hf-added condition. On the other hand, Fig. 3c and Table 3 and suggest that the addition of Y_2O_3 causes the processing regime to shift from keyhole to conduction-like mode, resulting in shallower melt pools. However, the observed lack of fusion (LoF) pores in Y_2O_3 samples (Fig. 8 in Appendix A) indicate that the processing regime was indeed LoF mode and not conduction-like mode, highlighting a potential trade-off in processability and necessitating adjustment of processing parameters for the admixed powders, especially Y_2O_3 added powder. Another interesting observation from the AE signal in Fig. 3c is that the signal amplitude decreased by an order of magnitude compared to Fig. 3a, suggesting a lower energy transfer to the sensor.

3.3 Post-mortem microstructural observations

For the standard CM247LC (Fig. 6a), SEM micrographs show two distinct types of cracking. Figure 6d shows a larger crack with a solidification structure, indicative of solidification cracking, while Fig. 6e highlights a smaller crack which is possibly HAZ liquation cracking. It is to be noted that the liquation cracking could not be observed in the *operando* radiographs most likely due to its smaller size as observed in Fig. 6e. It is often challenging to definitively distinguish these two types of cracking from microstructural analysis alone, as both can possibly exhibit evidence of solidification on their crack surfaces. The identified liquation crack in this study is similar in size to those described by Tang et al. [4], though it was not possible to visualize the crack surface to confirm similarity with the work from Phan et al. [5].

The addition of Hf drastically minimizes solidification cracking (Fig. 6b), which is consistent with the *operando* observations. There are also some solidification cracks (marked with black arrows) in Fig. 6b which were not observed in the radiographs (Fig. 3) or XCT images (Fig. 8 in Appendix A). Microstructural analysis reveals that Hf is present as partially melted particles dispersed throughout the matrix (Fig. 6h) and are marked by white arrows in Fig. 6b. These partially melted particles often display a core–shell-like structure, suggesting incomplete melting due to the high melting point of Hf [32] and partial diffusion of Hf into the surrounding matrix during processing. Furthermore, the shape of the partially melted particles suggests that they are on the bottom of the melt pool likely due to relatively high density of Hf (13.3 g/cm^3) [33] when compared to CM247LC (8.5 g/cm^3) [34].

A closer look at microstructure, especially in Fig. 6g indicates two features which have distinct contrast in BSE

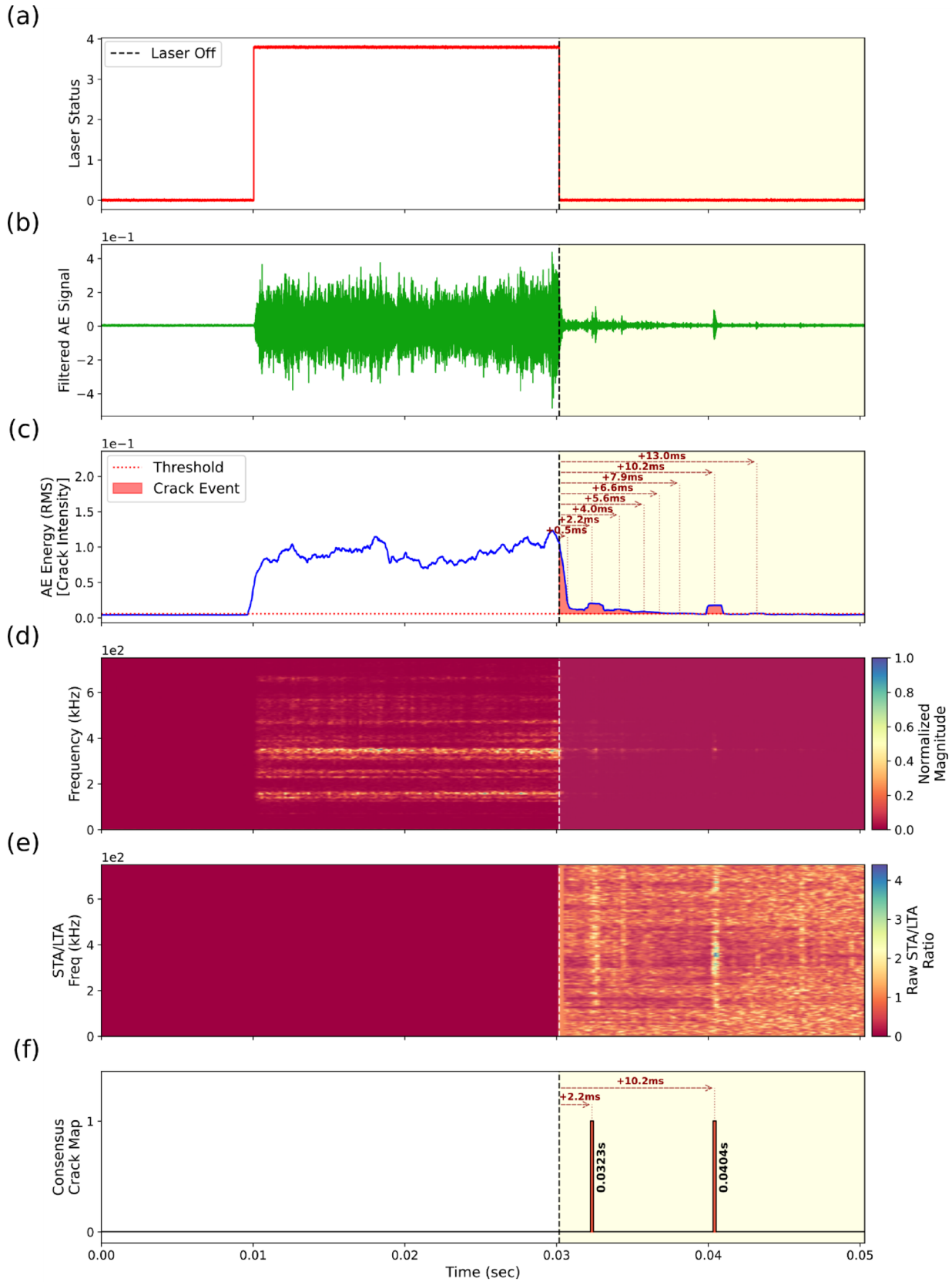
(a)
Laser Off
Laser Status
(b)
1e−1
Filtered AE Signal
(c)
1e−1
Threshold
Crack Event
AE Energy (RMS)
[Crack Intensity]
+13.0ms
+10.2ms
+7.9ms
+6.6ms
+5.6ms
+4.0ms
+2.2ms
+0.5ms
(d)
1e2
Frequency (kHz)
Normalized
Magnitude
(e)
1e2
STA/LTA
Freq (kHz)
Raw STA/LTA
Ratio
(f)
Consensus
Crack Map
+10.2ms
+2.2ms
0.0323s
0.0404s
Time (sec)

Fig. 5 Post-laser crack event analysis of acoustic emission (AE) signal for Standard CM247LC during PBF–LB: **a** laser trigger indicating the laser shut-off point, **b** filtered AE waveform, **c** moving RMS-based AE energy (crack intensity) with thresholded post-laser events and time delays, **d** normalized spectrogram showing temporal localization of acoustic activity, **e** STA/LTA time–frequency map highlighting transient post-laser disturbances, and **f** consensus crack map identifying dominant crack-associated events after laser shut-off

image. Feature '*i*' appears brighter in BSE contrast than feature '*j*' and has similar contrast to the primary MC carbides typically found in the interdendritic regions. EDS line scans performed across feature '*i*' in Fig. 6g confirm significant enrichment in Hf, Ta, and W, along with carbon, consistent with the formation of Hf-rich primary MC carbides typically found in CM247LC [2, 3, 35].

In directionally solidified superalloy castings, Hf has been shown to reduce grain boundary cracking, an effect attributed to its influence on the evolution of the liquid volume fraction during solidification, which in turn lowers solidification-induced strains [13]. It is highly probable that Hf imparts a similar beneficial effect in PBF–LB. The strong partitioning of Hf to the interdendritic regions during solidification, partially supported by EDS measurements, likely promotes a 'back-filling' effect or enhances grain boundary cohesion, thereby mitigating solidification cracking. This demonstrates the potential of incorporating Hf to minimize solidification cracking in CM247LC, contrasting with previous attempts in literature to eliminate Hf from this alloy [9, 10]. The observed partial melting of the admixed Hf powder further suggests that pre-alloyed CM247LC with a higher Hf content than the nominal composition needs to be further explored.

With the addition of Y_2O_3, minimized cracking was observed, though with different microstructural and processing implications than Hf. Figure 6c reveals poor bonding of the sample to the build plate and widespread LoF pores. This directly correlates with the shallower melt pools observed in the *operando* radiographs (Fig. 3c) that leads to an increased presence of LoF pores. Microstructural investigations (Fig. 6 c, k) further show that the Y_2O_3 additions were found in the form of micron-sized oxide agglomerates dispersed throughout the matrix. An EDS line scan (Fig. 6l) reveals that the Y_2O_3 had undergone some metallurgical interaction with the matrix material, resulting in enrichment of Hf, Al, and Ta in the agglomerated oxids. From previous studies [2, 36], some of these elements have been found as oxides in as-built condition in CM247LC possibly arising from residual oxygen from powder and/or process chamber. Therefore, it is likely that these elements most likely reacted with the Y_2O_3 to form complex oxide compounds that could float in the melt pool, as also documented in [18].

The transition from a deep keyhole to a shallow conduction melt pool, along with reduced AE amplitudes, suggests a fundamental alteration in the laser-material interaction caused by the Y_2O_3 addition. While this could be partially attributed to the slightly higher absorptivity of the Y_2O_3-containing powders (Fig. 2g) [37], the interaction is likely far more complex [38]. Microstructural analysis revealed that the nano-Y_2O_3 formed micron-sized agglomerates (Fig. 6 c, k). This behavior is likely due to the low density of Y_2O_3 (4.44 g/cm^3) and its significant surface tension mismatch with the molten nickel alloy, which would promote particles to float within the melt pool [18]. Additionally, the poor wettability of Y_2O_3 in molten nickel and strong Van der Waals' forces could contribute to the inhomogeneous dispersion of the nanoparticles [38]. A combination of these effects including floating, poor wettability, and agglomeration possibly led to the Y_2O_3 particles affecting the melt pool's interaction with the laser, resulting in the observed shallower melt pool geometry.

3.4 Understanding solidification behavior and crack inhibition

The real-time capability of *operando* observations was crucial for understanding the growth and kinetics of solidification cracks. By utilizing all observed solidification cracks from Supplementary Movie 1, the time stamps and corresponding crack lengths allowed for the calculation of solidification cracking speeds (Appendix B), which were found to be in the range of ~ 0.02 to 0.04 ms^{-1}. While direct comparative experimental data for such specific crack propagation rates in PBF–LB of superalloys is scarce in the literature, these measurements offer valuable quantitative insights into the dynamic nature of solidification cracking during additive manufacturing.

To further understand the underlying metallurgical mechanisms, non-equilibrium Scheil solidification simulations were employed. For this purpose, Scheil solidification simulations incorporating a solute trapping model were performed for all three alloy conditions. The use of Scheil solidification simulations, particularly with a solute trapping model [29], is a valuable approach for understanding non-equilibrium solidification in PBF–LB [39]. While acknowledging the simplified assumptions of the Scheil model (e.g., negligible solid-state diffusion), its ability to predict microsegregation and phase evolution during rapid cooling provides valuable first-order insights into solidification cracking susceptibility, consistent with its application in welding and other rapid solidification processes [40]. The solute trapping model is crucial for accurately representing PBF–LB conditions, as the rapid solidification velocities at the solid–liquid interface lead to non-equilibrium solute partitioning, a deviation from classic Scheil-Gulliver assumptions [39].

Table 3 Mean and standard deviation values of melt pool depth, melt pool width and melt pool aspect ratio from the radiographs

	Melt pool depth (μm)	Melt pool width (μm)	Melt pool aspect ratio
Standard	154 ± 17	23 ± 5	6.82 ± 1.85
Standard + 1 wt.% Hf	74 ± 6	45 ± 13	1.86 ± 0.84
Standard + 1 wt.% Y_2O_3	40 ± 10	104 ± 66	0.25 ± 0.03

Melt pool aspect ratio is given by the ratio of melt pool depth and melt pool width

Table 4 presents the liquidus temperature (T_L), solidus temperature (T_S), solidification range (ΔT), and solidification cracking index (SCI) based on Kou's model [40] for both equilibrium and Scheil solidification conditions. It is to be noted that although SCI has units of °C, it is useful for comparison purposes as an index [41]. The Scheil solidification curves, illustrating temperature versus mole fraction of solid (fs), are shown in Fig. 7. Please note that for Standard + Y_2O_3, the T_L (both equilibrium and Scheil) were taken at temperatures where the FCC_L12 (γ phase) is first observed. According to the Kou's model [40], SCI is defined as the absolute value of the slope of T vs. $(fs)^{1/2}$ specifically near the end of solidification ($(fs)^{1/2} = 1$). In this study, SCI values were averaged for the fs range of 0.8 to 0.99 (which gives $(fs)^{1/2}$ range of ~ 0.9 to 0.99). A higher SCI correlates with increased cracking susceptibility, as it indicates that the residual liquid phase is more resistant to feeding shrinkage during the final stages of solidification, thereby hindering grain bonding and increasing crack formation [40]. A sensitivity analysis was carried out by shifting the fs bounds by ± 0.05 and it was found that there were no alterations to the relative ranking based on SCI for the three alloys.

Firstly, comparing the equilibrium solidification ranges (Table 4) reveals no significant difference among the three alloys. However, the non-equilibrium Scheil simulations demonstrate clear distinctions. From Fig. 7 and Table 4, the Standard alloy exhibits the highest predicted susceptibility to cracking, characterized by a wider Scheil solidification range (ΔT_{scheil} = 302 °C) and the highest SCI value of 3437. A wider solidification range (ΔT_{scheil}) and a higher SCI are established indicators of increased solidification cracking susceptibility [40]. This is because of a protracted solidification interval, particularly with a steep temperature drop near the solidus (reflected by a high SCI), signifies a reduced ability of the remaining liquid films to accommodate thermally induced shrinkage strains. Such conditions lead to the formation of continuous liquid films at grain boundaries that are highly susceptible to tearing under tensile stresses, as observed in the *operando* experiments.

In contrast, Standard + Hf shows lower predicted cracking susceptibility (SCI = 2997 °C) despite a similar ΔT_{scheil} (318 °C). This reduced susceptibility is attributed to the flatter slope of its Scheil curve and, critically, the increased availability of liquid phase in the final stages of solidification (fs ~ 0.8 to 0.99) due to additional Hf remaining in the liquid after MC carbide formation (Fig. 9 in Appendix C). The strong partitioning of Hf to interdendritic regions, as confirmed by EDS and consistent with its tendency to form primary MC carbides [30], directly influences the liquid composition during solidification. This excess liquid facilitates improved 'back-filling' and thereby mitigates solidification cracking [1]. This mechanism, where the presence of a sufficient amount of liquid can flow into and heal incipient cracks, has been previously demonstrated for Hf-containing alloys in both casting [13] and other AM processes [14], effectively mitigating solidification cracking by reducing local tensile stresses in the mushy zone. This simulation finding strongly supports the experimentally observed crack reduction with Hf addition (Sect. 3.2).

The Standard + Y_2O_3 alloy exhibited the lowest predicted susceptibility (SCI = 855 °C) with a significantly narrower ΔT_{scheil} (186 °C). It is important to note that this particular simulation had a termination criterion of 0.06 fraction of liquid phase due to convergence issues. Therefore, linear extrapolation was done (indicated by green dotted line in Fig. 7) from fs of 0.94 to 0.99 to estimate the solidus temperature and calculate the SCI for this condition. Observing the non-equilibrium Scheil phase diagram (Fig. 9 in Appendix C) for the Y_2O_3 alloy predicts the formation of corundum phase (Al_2O_3), which could correspond to the experimental observation of complex oxides (Sect. 3.3). The absence of sigma phase in the Y_2O_3 containing alloy in the simulation also suggests a potentially beneficial influence on solidification.

While the Scheil simulations confirm a reduced inherent cracking susceptibility for the Y_2O_3 modified alloy due to a significantly narrower solidification range and lower SCI, our *operando* observations strongly indicate that the primary mechanism of crack mitigation is driven by a fundamental alteration of the melt pool geometry and processing mode (keyhole-like to conduction-like or LoF-like). This process-driven shift, likely influenced by the higher surface tension, poor wettability [16, 18, 38] along with increased absorptivity, creates solidification conditions inherently less prone to cracking. The lower SCI predicted by the Scheil model for

Fig. 6 SEM micrographs along with EDS for PBF–LB processed samples for **a** Standard. **d**, **e** magnified images of (**a**). **b** Standard + 1wt.% Hf. **f**, **g** indicates a region close to a solidification crack, The EDS line scans **i** and **j** were taken from the locations marked in micrograph (**g**). The inset **h** shows a higher magnification of the partially melted Hf particle **c** Standard + 1 wt.% Y_2O_3. The EDS line scan **l** was taken from the location marked in micrograph (**k**). SE refers to secondary electrons and BSE refers to backscattered electrons. Please note that the dashed line in **b**, **c** indicates the interface between the sample and the build plate

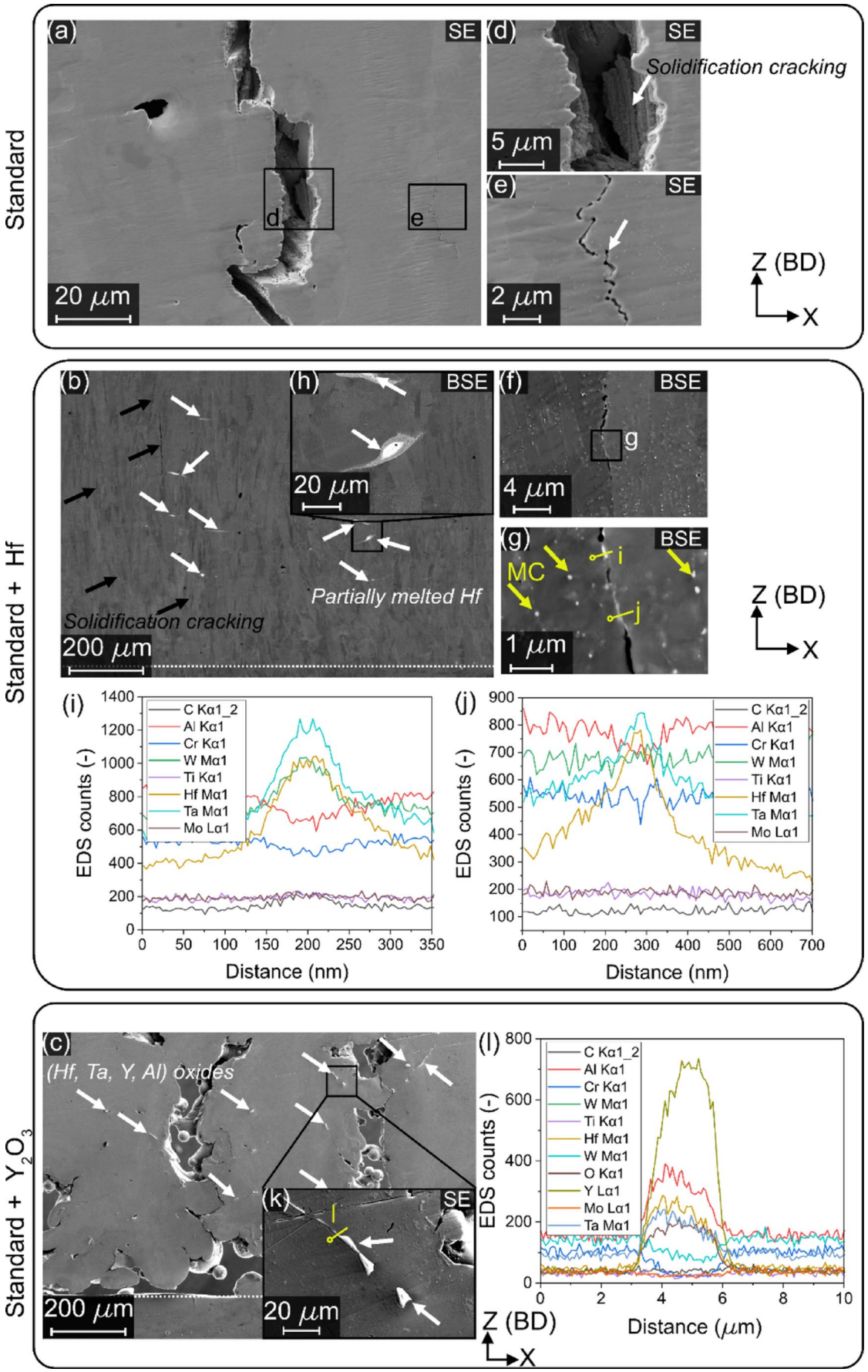
Standard
(a)
SE
d
e
20 μm
(d)
SE
Solidification cracking
5 μm
(e)
SE
2 μm
Z (BD)
X
Standard + Hf
(b)
(h)
BSE
20 μm
Partially melted Hf
Solidification cracking
200 μm
(f)
BSE
g
4 μm
(g)
BSE
MC
i
j
1 μm
Z (BD)
X
(i)
EDS counts (-)
Distance (nm)
C Kα1_2
Al Kα1
Cr Kα1
W Mα1
Ti Kα1
Hf Mα1
Ta Mα1
Mo Lα1
(j)
EDS counts (-)
Distance (nm)
Standard + Y2O3
(c)
(Hf, Ta, Y, Al) oxides
(k)
SE
l
200 μm
20 μm
(l)
EDS counts (-)
Distance (μm)
C Kα1_2
Al Kα1
Cr Kα1
W Mα1
Ti Kα1
Hf Mα1
W Mα1
O Kα1
Y Lα1
Mo Lα1
Ta Mα1
Z (BD)
X

Table 4 Liquidus temperature T_L, solidus temperature T_S, solidification range ΔT for equilibrium (*eq*) and Scheil solidification simulations from Thermo-Calc 2025b along with solidification cracking index (SCI) based on Kou's model [40] for the three alloys for fraction of solid between 0.8 and 0.99

	$T_{L,eq}$ (°C)	$T_{S,eq}$ (°C)	ΔT_{eq} (°C)	$T_{L,scheil}$ (°C)	$T_{S,scheil}$ (°C)	ΔT_{scheil} (°C)	SCI (°C)
Standard	1407	1320	87	1384	1082	302	3437
Standard + Hf	1404	1306	98	1371	1053	318	2997
Standard + Y_2O_3	1407	1321	86	1396	1210	186	855

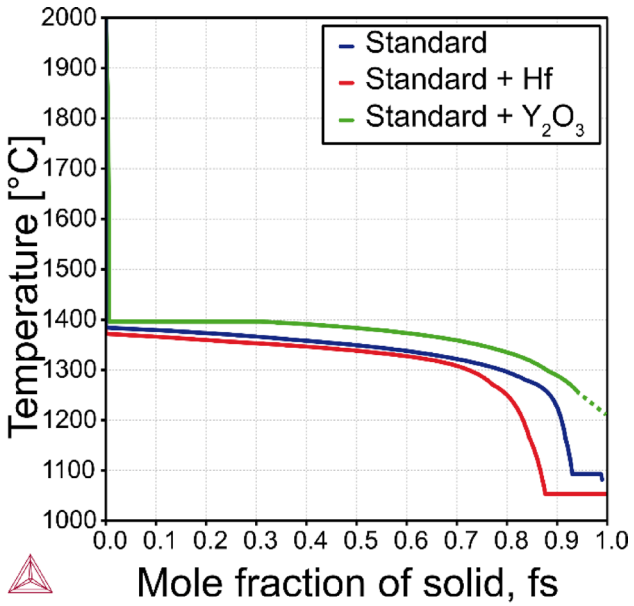

Fig. 7 Temperature vs mole fraction of solid from Scheil solidification simulations with solute trapping using Thermo-Calc 2025b (TCNI13 database) for the three alloys considered. The scan speed of 200 mm/s and the angle between scanning direction and solidification direction ($\alpha = 45°$) were used. Note: Standard + Y_2O_3 simulation was terminated at fraction of solid of 0.94 due to convergence issue and the green dotted line is the linear interpolation

the Y_2O_3 alloy is probably complementary to this observed shift in processing regime. However, the mechanism behind the narrower Scheil solidification results for Y_2O_3 modified powder requires further work.

3.5 Limitations and future work

A notable challenge encountered was the identification of crack events from the AE sensor during the active laser scan. While AE monitoring successfully correlated with crack formation after the laser pass, the high background noise inherent to the active laser processing made real-time crack detection during the scan difficult. Deconvoluting cracking signals from other transient events remains a key area of ongoing work.

Regarding the Y_2O_3-containing alloy, XCT observations (Appendix A, Fig. 8) revealed inhomogeneity in lack-of-fusion defects, suggesting that the dispersion of nano-Y_2O_3 within the initial powder might not have been uniform. This indicates that achieving consistent and repeatable crack mitigation with nano-Y_2O_3 additions is challenging. Improved powder mixing and PBF–LB processing parameters are therefore crucial for ensuring a homogeneous dispersion and consistent material properties. Furthermore, process optimization is needed to compensate for the increase in lack-of-fusion defects observed, a key trade-off of this mitigation strategy.

Beyond these specific challenges, the broader industrial application of nanoparticle-dispersed superalloys presents complex hurdles. The presence of nanoparticles like Y_2O_3 can hinder grain growth (demonstrated for IN625 with Y_2O_3 additions) [37] during subsequent heat treatments (e.g., solution and aging). Grain growth is essential for developing the required microstructure and mechanical properties, especially high temperature creep performance. This makes the Hf-modified route more attractive from an industrial standpoint. However, the observed partial melting of the Hf particles suggests that exploring a pre-alloyed powder is of high interest for this route.

Finally, it is important to note that the experiment was performed on a groove/thin wall with slow scanning speeds (200 mm/s) and the typical scanning speeds employed in production-ready industrial machines are in the range of 1000–2000 mm/s. In bulk components with higher scan speeds, the melt-pool aspect ratio, degree of keyholing and thermal gradients can differ substantially from the present configuration in the MiniSLM, which may modify both the crack initiation and propagation and the solidification behavior. Nevertheless, the two mitigation mechanisms identified here, (i) enhanced Hf segregation and back-filling at the end of solidification and (ii) Y_2O_3-induced shift from keyhole to shallower conduction-like mode melt pools are governed by local solidification and melt-pool physics and are therefore expected to remain qualitatively relevant under industrial scan strategies. Future work on multi-layer bulk builds at 1000–2000 mm/s is crucial to quantify how the mechanisms interact with realistic scan strategies.

4 Conclusions

This study explores the *operando* radiography and synchronized acoustic emission (AE) monitoring to investigate dynamic cracking behavior during powder bed fusion–laser beam (PBF–LB) of crack-prone CM247LC superalloy. Crack mitigation strategies through separate additions of 1 wt.% Hf and 1 wt.% Y_2O_3 were explored, with insights

further deepened by post-mortem microstructural analysis and non-equilibirum Scheil solidification simulations. The following conclusions can be drawn from the study:

- *Operando* observations demonstrate that the Standard CM247LC is highly susceptible to solidification cracking. The solidification cracking speeds were measured to be ~ 0.02 to 0.04 ms^{-1}. Additions of 1 wt.% Hf and 1 wt.% Y_2O_3 effectively mitigate cracking under identical processing conditions.
- For CM247LC + 1 wt.% Hf, crack mitigation is primarily attributed to the increased segregation of Hf to the interdendritic regions, leading to enhanced liquid feeding and grain boundary cohesion ('backfilling effect'), however the change in melt pool depth could also be a contributing factor. Non-equilibrium Scheil simulations corroborate this by predicting increased liquid availability in the final stages of solidification, resulting in a lower solidification cracking index (SCI) for the Hf-modified alloy. This highlights a mechanism of alloy design that directly enhances resistance to solidification cracking.
- For CM247LC + 1 wt.% Y_2O_3, crack reduction is associated with a fundamental shift in the processing regime from keyhole to shallower conduction-like/LoF-like mode. While Scheil simulations for this alloy predict the lowest solidification cracking index (SCI) and a narrower solidification range, the dominant mechanism for crack mitigation appears to be the shift in processing regime.
- Synchronized AE signals confirm that events occurring after the laser pass correlate with the crack formation in CM247LC. The absence of such AE events in the Hf- and Y_2O_3-containing alloys further validates their enhanced resistance to solidification cracking.
- The crack-associated AE response in Standard CM247LC was mainly concentrated within 150–450 kHz, with the strongest contribution around 300–450 kHz. However, since the post-laser AE bursts occurred within the same dominant frequency window as the broader bulk laser–material interaction response, crack identification was not based on a unique crack-specific frequency band alone, but on the transient burst morphology, localized post-laser timing, and correlation with operando radiographic crack evolution.

Appendices

Appendix 1: X-ray computed tomography of samples

See Fig. 8.

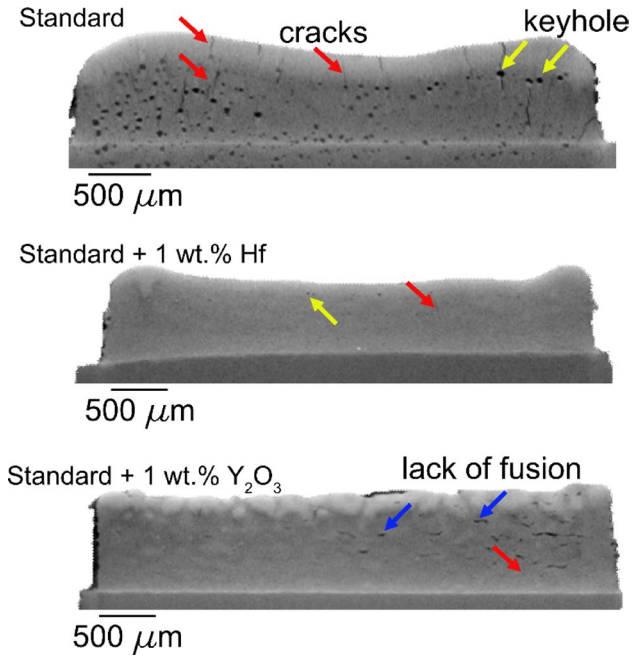

Fig. 8 Single projection of X-ray computed tomography (XCT) of the samples printed during the operando investigation

Appendix 2: Dataset for calculating kinetics of solidification cracking

$$Solidification\ cracking\ speed\ (\mathrm{ms}^{-1}) = \frac{Crack\ length}{t_2 - t_1} \times 10^{-3}$$

See Table 5.

Table 5 Parameters showing the cracks and their characteristics used for calculated solidification cracking speed

	t1 (ms)	t2 (ms)	Crack length (μm)	Solidification cracking speed (10^{-3} m s^{-1})
Crack 1	1.4	6.2	122	25.42
Crack 2	2.4	6.4	102	25.69
Crack 3	6	9.4	66	19.50
Crack 4	18.5	22.5	150	37.62

t1 is the initial timestamp and t2 is the final timestamp for the crack to have grown

Appendix 3: Thermo-calc simulations

See Table 6 and Fig. 9.

Table 6 Composition (in wt.%) used for simulations in Thermo-Calc 2025b

	Cr	Co	Mo	C	W	Hf	Ta	Ti	Al	Y	O	Zr	B	Ni
Standard	8	9.3	0.5	0.06	9.7	1.3	3.2	0.8	5.6	–	–	0.009	0.01	61.521
Standard + 1 wt.% Hf	7.920	9.207	0.495	0.059	9.603	2.287	3.168	0.792	5.544	–	–	0.009	0.01	60.906
Standard + 1 wt.% Y_2O_3	7.920	9.207	0.495	0.059	9.603	1.287	3.168	0.792	5.544	0.787	0.213	0.009	0.01	60.906

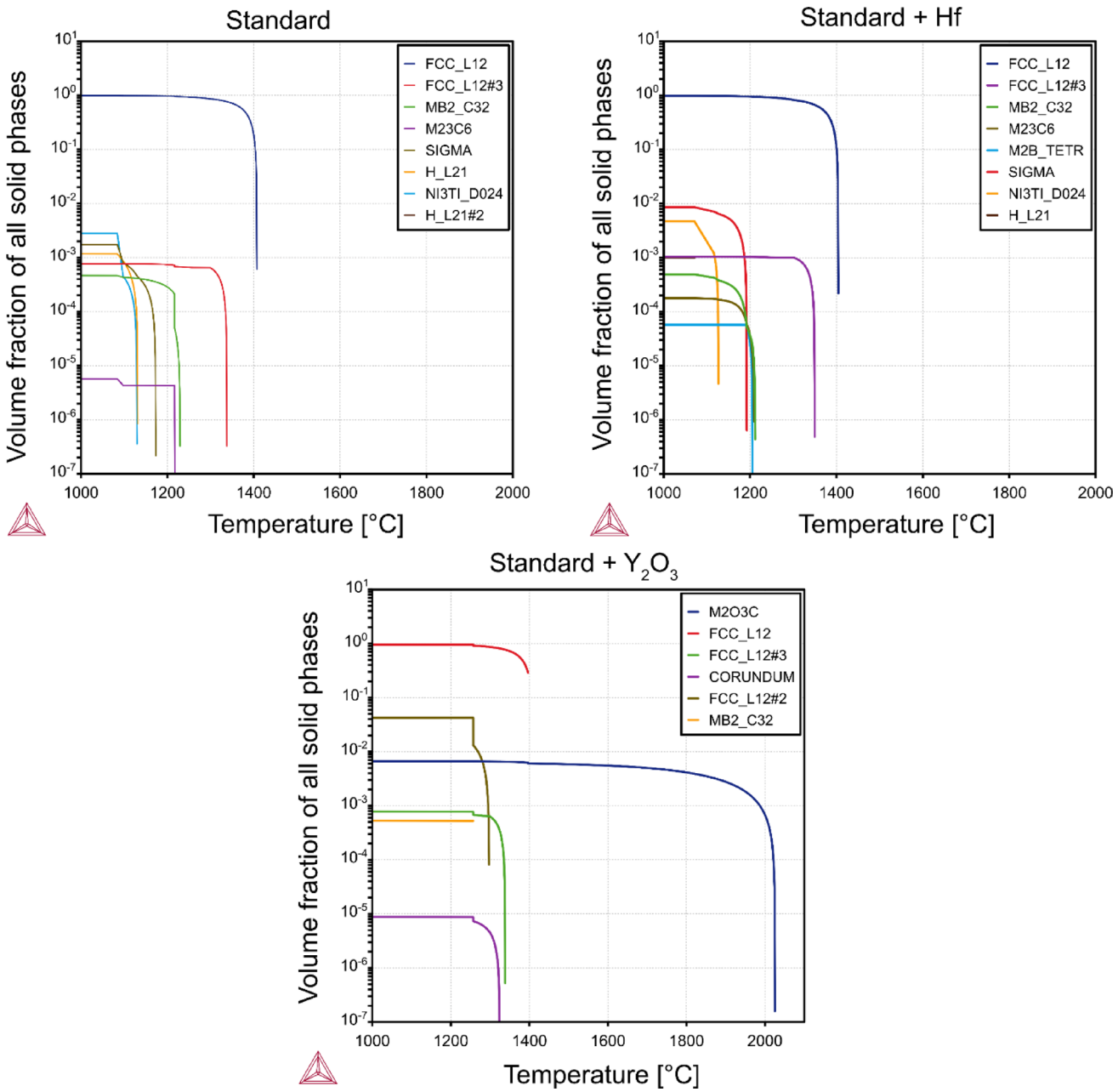

Fig. 9 Volume fraction of solid phases calculated from non-equilibrium Scheil solidification simulations using Thermo-Calc 2025b software using the TCNI13 database. FCC_L12: γ phase, FCC_L12#2: γ′ phase and FCC_L12#3: MC carbide

Supplementary Information The online version contains supplementary material available at https://doi.org/10.1007/s40964-026-01876-5.

Acknowledgements This work has been performed in the framework of MAGDA (Materials for green hydrogen fueled gas turbines through additive manufacturing) project and the Centre for Additive Manufacturing – Metal (CAM2), both supported by Swedish Governmental Agency for Innovation Systems (Vinnova). Gowtham Soundarapandiyan, Efthymios Polatidis and Steven Van Petegem acknowledge the PSI CROSS project "Enabling Acoustic Emission for monitoring Selective Laser Melting guided by in situ synchrotron X-ray diffraction experiments". The Paul Scherrer Institut is acknowledged for provision of X-ray beam time at the TOMCAT beamline (proposal No. 20220659). Ahmed Fardan and Gowtham Soundarapandiyan acknowledge Thiemo Benthien (University of Bremen) for image analysis of the supplementary videos.

Author contributions A.F: Conceptualization, Formal analysis, Investigation, Visualization, Writing—original draft, Writing—review & editing. G.S: Conceptualization, Formal analysis, Investigation, Visualization, Writing—review & editing. V.P: Conceptualization, Formal analysis, Investigation, Visualization, Writing—review & editing. S.V.P: Conceptualization, Funding acquisition, Investigation, Resources, Supervision, Writing—review & editing. E.P: Conceptualization, Investigation, Resources, Supervision, Writing—review & editing, Funding acquisition. S.K: Investigation, Visualization, Writing—review & editing. S.G: Conceptualization, Investigation, Writing—review & editing. C.P: Investigation, Writing—review & editing. F.M: Investigation, Resources, Writing—review & editing. B.M: Investigation, Resources, Visualization, Writing—review & editing. A.P: Investigation, Visualization, Writing—review & editing. H.B: Conceptualization, Supervision, Writing—review & editing. E.H: Conceptualization, Supervision, Resources, Writing—review & editing, Funding acquisition.

Funding Open access funding provided by Chalmers University of Technology.

Data availability The data supporting the findings of this paper are available from the corresponding author on reasonable request. For those interested, the dataset and code associated with this study are available at the following repository: https://gitlab.utu.fi/vpsora/Additive-Manufacturing-CM247-Subsurface-Process-Monitoring.

Declarations

Competing interests The authors declare no competing interests.

References

1. Kou S (2003) Welding metallurgy., 2. ed. Wiley
2. Fardan A, Fazi A, Peng RL, Mishurova T, Thuvander M, Bruno G, Brodin H, Hryha E (2024) Fine-tuning melt pools and microstructures: taming cracks in powder bed fusion-laser beam of a non-weldable Ni-base superalloy. Materialia 34:102059. https://doi.org/10.1016/j.mtla.2024.102059
3. Fardan A, Fazi A, Schröder J, Mishurova T, Deckers T, Bruno G, Thuvander M, Markström A, Brodin H, Hryha E (2025) Microstructure tailoring for crack mitigation in CM247LC manufactured by powder bed fusion–laser beam. Addit Manuf 99:104672. https://doi.org/10.1016/j.addma.2025.104672
4. Tang YT, Panwisawas C, Ghoussoub JN, Gong Y, Clark JWG, Németh AAN, McCartney DG, Reed RC (2021) Alloys-by-design: application to new superalloys for additive manufacturing. Acta Mater 202:417–436. https://doi.org/10.1016/j.actamat.2020.09.023
5. Phan MAL, Dew O, Todd I (2024) Predictive process diagram for parameters selection in laser powder bed fusion to achieve high-density and low-cracking built parts. Addit Manuf 85:104145. https://doi.org/10.1016/j.addma.2024.104145
6. Ghasemi-Tabasi H, de Formanoir C, Van Petegem S, Jhabvala J, Hocine S, Boillat E, Sohrabi N, Marone F, Grolimund D, Van Swygenhoven H, Logé RE (2022) Direct observation of crack formation mechanisms with operando laser powder bed fusion X-ray imaging. Addit Manuf 51:102619. https://doi.org/10.1016/j.addma.2022.102619
7. Carter LN, Attallah MM, Reed RC (2012) Laser powder bed fabrication of nickel-base superalloys: influence of parameters; characterisation, quantification and mitigation of cracking. In: Proceedings of the international symposium on superalloys, pp 577–586. https://doi.org/10.7449/2012/superalloys_2012_577_586
8. Adegoke O, Andersson J, Brodin H, Pederson R (2020) Influence of laser powder bed fusion process parameters on voids, cracks, and microhardness of nickel-based superalloy alloy 247LC. Materials (Basel) 13:1–23. https://doi.org/10.3390/MA13173770
9. Griffiths S, Ghasemi Tabasi H, Ivas T, Maeder X, De Luca A, Zweiacker K, Wróbel R, Jhabvala J, Logé RE, Leinenbach C (2020) Combining alloy and process modification for micro-crack mitigation in an additively manufactured Ni-base superalloy. Addit Manuf 36:101443. https://doi.org/10.1016/j.addma.2020.101443
10. Markanday JFS, Christofidou KA, Miller JR, Livera ER, Jones NG, Pickering EJ, Li W, Pardhi Y, Jones CN, Stone HJ (2023) The microstructural evolution of CM247LC manufactured through laser powder bed fusion. Metall Mater Trans A. https://doi.org/10.1007/s11661-022-06939-0
11. Li L, Wu Y, Hou J, Gao S, Zhou L (2024) The effect of Hafnium on the microstructure and tensile property in a Ni-based superalloy. J Mater Res Technol 30:2977–2985. https://doi.org/10.1016/j.jmrt.2024.04.049
12. Ou M, Ma Y, Hou K, Liu K (2022) Effect of hafnium content on the microstructural evolution and stress rupture properties of K4750 nickel-based superalloy. J Alloys Compd 916:165473. https://doi.org/10.1016/j.jallcom.2022.165473
13. Zhang J, Singer RF (2002) Effect of hafnium on the castability of directionally solidified nickel-base superalloys. Z Metallkd 93:806–811. https://doi.org/10.3139/146.020806
14. Yu Z, Guo C, Han S, Hu X, Cao L, Xu Z, Ding H, Zhu Q (2021) The effect of Hf on solidification cracking inhibition of IN738LC processed by selective laser melting. Mater Sci Eng A 804:140733. https://doi.org/10.1016/j.msea.2021.140733
15. Zhou W, Zhu G, Wang R, Yang C, Tian Y, Zhang L, Dong A, Wang D, Shu D, Sun B (2020) Inhibition of cracking by grain boundary modification in a non-weldable nickel-based superalloy processed

by laser powder bed fusion. Mater Sci Eng A 791:139745. https://doi.org/10.1016/j.msea.2020.139745
16. Wei B, Liu Z, Cao B, Nong B, Zhang Y, Ren Y, Zhou H, Wei S (2021) Cracking inhibition of nano-TiC reinforced René 104 superalloy fabricated by selective laser melting. J Alloys Compd 881:160413. https://doi.org/10.1016/j.jallcom.2021.160413
17. Guo C, Yu Z, Hu X, Li G, Zhou F, Xu Z, Han S, Zhou Y, Ward RM, Zhu Q (2022) Y2O3 nanoparticles decorated IN738LC superalloy manufactured by laser powder bed fusion: cracking inhibition, microstructures and mechanical properties. Compos B Eng 230:109555. https://doi.org/10.1016/j.compositesb.2021.109555
18. Kenel C, De Luca A, Joglekar SS, Leinenbach C, Dunand DC (2021) Evolution of Y_2O_3 dispersoids during laser powder bed fusion of oxide dispersion strengthened Ni-Cr-Al-Ti γ/γ' superalloy. Addit Manuf 47:102224. https://doi.org/10.1016/j.addma.2021.102224
19. Song JY, Dass A, Moridi A, McLaskey GC (2024) Detection of defects during laser-powder interaction by acoustic emission sensors and signal characteristics. Addit Manuf 82:104035. https://doi.org/10.1016/j.addma.2024.104035
20. Raeker EB, Tulshibagwale N, Mullin KM, Lamb JD, Pollock TM (2025) Detection and classification of cracking via acoustic emission during laser-melting screening for additive manufacturing. JOM 77:7274–7286. https://doi.org/10.1007/s11837-025-07642-2
21. Esmaeilzadeh R, Pandiyan V, Van Petegem S, Van der Meer M, Nasab MH, de Formanoir C, Jhabvala J, Navarre C, Schlenger L, Richter R, Casati N, Wasmer K, Logé RE (2024) Acoustic emission signature of martensitic transformation in laser powder bed fusion of Ti6Al4V-Fe, supported by operando X-ray diffraction. Addit Manuf 96:104562. https://doi.org/10.1016/j.addma.2024.104562
22. Navarre C, Hearn W, Van der Meer M, Schlenger L, Vaerenberg R, Mari N, Esmaeilzadeh R, Jamili AM, Pandiyan V, Van Petegem S, Logé RE (2026) Exploring real-time monitoring of laser-induced recrystallization using acoustic emissions. Opt Laser Technol 195:114591. https://doi.org/10.1016/j.optlastec.2025.114591
23. Ansari MJ, Roccisano A, Arcondoulis EJG, Schulz C, Schläfer T, Hall C (2025) Relationship between associated acoustic emission and crack position during directed energy deposition of a metal matrix composite. J Manuf Process 147:177–190. https://doi.org/10.1016/j.jmapro.2025.05.015
24. Bevans BD, Riensche A, Carrington A, Deshmukh K, Darji M, Plotnikov Y, Sions J, Snyder K, Hass D, Rao P (2025) In-process monitoring of part quality in laser powder bed fusion additive manufacturing process using acoustic emission sensors. J Manuf Sci Eng. https://doi.org/10.1115/1.4067848
25. Hocine S, Van Swygenhoven H, Van Petegem S, Chang CST, Maimaitiyili T, Tinti G, Sanchez DF, Grolimund D, Casati N (2020) Operando X-ray diffraction during laser 3D printing. Mater Today 34:30–40. https://doi.org/10.1016/j.mattod.2019.10.001
26. Hocine S, Van Petegem S, Frommherz U, Tinti G, Casati N, Grolimund D, Van Swygenhoven H (2020) A miniaturized selective laser melting device for operando X-ray diffraction studies. Addit Manuf 34:101194. https://doi.org/10.1016/j.addma.2020.101194
27. Vallen Systeme, VS370-A3 (n.d.) https://www.vallen.de/sensors/high-frequencs-sensors-400-khz/vs370-a3/
28. Mokso R, Schlepütz CM, Theidel G, Billich H, Schmid E, Celcer T, Mikuljan G, Sala L, Marone F, Schlumpf N, Stampanoni M (2017) GigaFRoST: the gigabit fast readout system for tomography. J Synchrotron Radiat 24:1250–1259. https://doi.org/10.1107/S1600577517013522
29. Aziz MJ, Kaplan T (1988) Continuous growth model for interface motion during alloy solidification. Acta Metall 36:2335–2347. https://doi.org/10.1016/0001-6160(88)90333-1
30. Hu P, Liu Z, Zhang H, Li Y, Zhou Q, Xie J (2024) Effect of remelting on cracking of Inconel 939 fabricated via laser powder bed fusion. Mater Charact 214:114087. https://doi.org/10.1016/j.matchar.2024.114087
31. Xi X, Lin D, Song X, Wei H, Yan M, Luo W, Chen B, Tan C, Dong Z, Minami F (2025) In-situ remelting induced healing of cracks and strength-ductility synergy in additively manufactured Haynes 230 alloy. Addit Manuf 98:104638. https://doi.org/10.1016/j.addma.2025.104638
32. Rosenberg H, Sharif A (2016) Hafnium production and refining. In: Reference Module in Materials Science and Materials Engineering. Elsevier. https://doi.org/10.1016/b978-0-12-803581-8.02565-0
33. AZoM (2001) Hafnium (Hf)—properties and applications
34. Harris K, Erickson G, Schwer R (1984) MAR M247 derivations—CM 247 LC DS alloy and CMSX single crystal alloys: properties and performance. Superalloys 1984:221–230. https://doi.org/10.7449/1984/Superalloys_1984_221_230
35. Adegoke O, Kumara C, Thuvander M, Deirmina F, Andersson J, Brodin H, Harlin P, Pederson R (2023) Scanning electron microscopy and atom probe tomography characterization of laser powder bed fusion precipitation strengthening nickel-based superalloy. Micron 171:103472. https://doi.org/10.1016/j.micron.2023.103472
36. Divya VD, Muñoz-Moreno R, Messé OMDM, Barnard JS, Baker S, Illston T, Stone HJ (2016) Microstructure of selective laser melted CM247LC nickel-based superalloy and its evolution through heat treatment. Mater Charact 114:62–74. https://doi.org/10.1016/j.matchar.2016.02.004
37. Li M, Wang L, Yang H, Zhang S, Lin X, Huang W (2022) Microstructure and mechanical properties of Y2O3 strengthened Inconel 625 alloy fabricated by selective laser melting. Mater Sci Eng A. https://doi.org/10.1016/j.msea.2022.143813
38. Yu WH, Sing SL, Chua CK, Kuo CN, Tian XL (2019) Particle-reinforced metal matrix nanocomposites fabricated by selective laser melting: a state of the art review. Prog Mater Sci 104:330–379. https://doi.org/10.1016/j.pmatsci.2019.04.006
39. Porter DA, Easterling KE, Sherif MY (2009) Phase transformations in metals and alloys. https://doi.org/10.1201/9781439883570
40. Kou S (2015) A criterion for cracking during solidification. Acta Mater 88:366–374. https://doi.org/10.1016/j.actamat.2015.01.034
41. Michael FN, Sowards JW, Marshall GC (2023) Numerical study of solidification crack susceptibility in novel refractory alloy systems. https://ntrs.nasa.gov/api/citations/20230002218/downloads/NASA_TM_20230002218.pdf. Accessed Aug 11 2025

Authors and Affiliations

Ahmed Fardan[1] · Gowtham Soundarapandiyan[1,2] · Vigneashwara Pandiyan[3,4] · Steven Van Petegem[5] · Efthymios Polatidis[6] · Sofia Kazi[1] · Sneha Goel[5,7] · Camille Pauzon[1,8] · Federica Marone[9] · Bharat Mehta[10] · Annapaola Parrilli[11] · Håkan Brodin[1,12] · Eduard Hryha[1]

✉ Ahmed Fardan
fardan@chalmers.se

Gowtham Soundarapandiyan
gowsou@chalmers.se

Vigneashwara Pandiyan
vigneashwara.solairajapandiyan@utu.fi

Steven Van Petegem
steven.vanpetegem@psi.ch

Efthymios Polatidis
polatidis@upatras.gr

Sofia Kazi
sofiakaz@chalmers.se

Sneha Goel
sneha.goel@vtt.fi

Camille Pauzon
pauzon@chalmers.se

Federica Marone
federica.marone@psi.ch

Bharat Mehta
bharat@thermocalc.com

Annapaola Parrilli
Annapaola.Parrilli@empa.ch

Håkan Brodin
hakan.brodin@siemens-energy.com

Eduard Hryha
hryha@chalmers.se

[1] Department of Mechanical Engineering, Chalmers University of Technology, Rännvägen 2A, 41296 Göteborg, Sweden

[2] Applied Materials Group, Laboratory for Neutron Scattering and Imaging, Paul Scherrer Institute (PSI), Forschungsstrasse 111, 5232 Villigen, Switzerland

[3] Laboratory for Advanced Materials Processing (LAMP), Swiss Federal Laboratories for Materials Science and Technology (Empa), Feuerwerkerstrasse 39, 3602 Thun, Switzerland

[4] Department of Mechanical and Materials Engineering, University of Turku, Joukahaisenkatu 3-5, 20520 Turku, Finland

[5] Structure and Mechanics of Advanced Materials, Paul Scherrer Institute (PSI), Forschungsstrasse 111, 5232 Villigen, Switzerland

[6] Laboratory of Technology and Strength of Materials, Department of Mechanical Engineering and Aeronautics, University of Patras, 26504 Patras, Greece

[7] Advanced Materials for Nuclear Energy, VTT Technical Research Centre of Finland, 02150 Espoo, Finland

[8] CNRS, Grenoble INP, SIMaP laboratory, Université Grenoble Alpes, 38000 Grenoble, France

[9] Swiss Light Source, Paul Scherrer Institute (PSI), 5232 Villigen, Switzerland

[10] Thermo-Calc Software (Sweden), Råsundavägen 18A, 16967 Solna, Sweden

[11] Center for X-Ray Analytics, Swiss Federal Laboratories for Materials Science and Technology (Empa), 8600 Dübendorf, Switzerland

[12] Siemens Energy AB, 612 83 Finspång, Sweden